Estimating and leveraging protein diffusion on ion-exchange resin surfaces

Ohnmar Khanal[a], Vijesh Kumar[a], Fabrice Schlegel[b], and Abraham M. Lenhoff[a,1]

[a]Department of Chemical and Biomolecular Engineering, University of Delaware, Newark, DE 19716; and [b]Process Development, Amgen, Cambridge, MA 02141

Edited by Andrew Zydney, The Pennsylvania State University, University Park, PA, and accepted by Editorial Board Member Pablo G. Debenedetti February 18, 2020 (received for review December 6, 2019)

Protein mobility at solid–liquid interfaces can affect the performance of applications such as bioseparations and biosensors by facilitating reorganization of adsorbed protein, accelerating molecular recognition, and informing the fundamentals of adsorption. In the case of ion-exchange chromatographic beads with small, tortuous pores, where the existence of surface diffusion is often not recognized, slow mass transfer can result in lower resin capacity utilization. We demonstrate that accounting for and exploiting protein surface diffusion can alleviate the mass-transfer limitations on multiple significant length scales. Although the surface diffusivity has previously been shown to correlate with ionic strength (IS) and binding affinity, we show that the dependence is solely on the binding affinity, irrespective of pH, IS, and resin ligand density. Different surface diffusivities give rise to different protein distributions within the resin, as characterized using confocal microscopy and small-angle neutron scattering (length scales of micrometer and nanometer, respectively). The binding dependence of surface diffusion inspired a protein-loading approach in which the binding affinity, and hence the surface diffusivity, is modulated by varying IS. Such gradient loading increased the protein uptake efficiency by up to 43%, corroborating the importance of protein surface diffusion in protein transport in ion-exchange chromatography.

surface diffusion | protein–surface interaction | protein transport | dynamic binding capacity | small-angle neutron scattering

Protein diffusion on surfaces is prevalent in biological events such as the diffusion of reparatory protein complexes on dsDNA for break repair (1) and of surface-mobile amyloid-β peptides in enhancing fibril formation, associated with neurogenerative diseases (2, 3). Protein surface diffusion can also impact the performance of microcapillary immunosensors (4, 5) and of label-free technologies such as surface plasmon resonance sensors (6) and chromatography (7). The phenomenon has also been invoked in analysis of preparative ion-exchange chromatography (IEX) of proteins, an enabling technology for high-selectivity adsorptive purification of proteins based on differences in their charge properties. The chromatographic beads used for IEX feature narrow, tortuous pores to maximize the surface-to-volume ratio, making intraparticle diffusion the rate-limiting factor in protein adsorption. Inside the particle, diffusion can occur in the liquid pore space (pore diffusion) and potentially on the resin surface (surface diffusion), as shown in the simplified schematic in *SI Appendix*, Fig. S1 and refs. 8 and 9. On the particle length scale, such surface diffusion can enhance the protein uptake rate and consequently also the process efficiency. Surface diffusion can also increase the local capacity for protein adsorption beyond what is anticipated for random sequential adsorption by allowing rearrangement of adsorbed molecules to improve the packing efficiency. In both these cases, modulation of the protein diffusivity on the surface (D_s) can provide an additional means to improve performance. However, protein surface diffusion is not sufficiently well accepted to be used by design to enhance performance.

Surface diffusion of small molecules (10–12) and polymers (13–16), unlike that of proteins, has been widely reported in liquid–solid systems. In reverse-phase liquid chromatography, hydrocarbons have been reported to diffuse at the interfacial region near the end of the alkyl chains of the stationary phase (17–21). Surface diffusion of proteins is more difficult to study due to their size and anisotropic structures, as well as their stronger adsorption. For conditions relevant to IEX, where protein-surface attraction is governed mainly by electrostatic interactions, the surface diffusivity of bovine serum albumin (8, 22, 23) and ferritin (24) on flat charged surfaces has been measured. However, for structurally intact IEX particles, direct observation of the surface is difficult and surface diffusion has been inferred with the aid of mechanistic chromatographic modeling (9, 25). Differences in protein uptake patterns among resins of different structures, observed by confocal microscopy, could be explained by the presence of surface diffusion but with a variable D_s (26, 27). For mechanistic models accounting for surface diffusion, the dependence of D_s on protein concentration (12, 28, 29), ionic strength (8, 25), and binding strength (9) has been reported, warranting a consistent and more comprehensive investigation into protein surface diffusion in IEX. An extensive understanding of protein surface diffusion in IEX can inspire engineering measures that can reduce losses associated with what the Food and Drug Administration describes as inefficient and wasteful manufacturing (30) of increasingly prevalent (31) and costly therapeutic proteins.

Significance

Direct measurement of protein diffusion at a solid–liquid interface, unlike that in a bulk liquid phase, is challenging, particularly in complex adsorbent geometries. As a result there is disagreement as to whether surface diffusion contributes significantly to protein transport into porous ion-exchange chromatography (IEX) beads. We provide complementary evidence supporting the role of surface diffusion in protein transport into IEX media and show that the diffusivity depends explicitly on adsorption affinity. Exploiting this relationship, we further present an innovative procedure for loading protein onto a column that increases the column productivity by 43% for purification of a monoclonal antibody. We therefore provide a multipronged approach for investigating protein surface diffusion and validate its significance in protein transport.

Author contributions: O.K., V.K., and A.M.L. designed research; O.K. and V.K. performed research; O.K., V.K., F.S., and A.M.L. analyzed data; and O.K. and A.M.L. wrote the paper.

The authors declare no competing interest.

This article is a PNAS Direct Submission. A.Z. is a guest editor invited by the Editorial Board.

[1]To whom correspondence may be addressed. Email: lenhoff@udel.edu.

This article contains supporting information online at https://www.pnas.org/lookup/suppl/doi:10.1073/pnas.1921499117/-/DCSupplemental.

First published March 16, 2020.

Bridging a gap between idealized investigations and practical applications, we have investigated the role of surface diffusion in the uptake of an industrially relevant protein, a monoclonal antibody (mAb), onto commercial resins. We probed the variability of protein D_s and its dependence on parameters pertaining to protein adsorption, such as buffer pH, ionic strength (IS), and the adsorbent ligand density. Using our findings, we developed a gradient method of protein loading that significantly increases resin utility. As was done in the prior studies noted above, we estimated D_s using a mechanistic column model. However, the impact of surface diffusion on protein uptake was also investigated via microscale observations by confocal microscopy and nanoscale structure characterization by small-angle neutron scattering (SANS) to corroborate and expand the model insights. This multipronged approach informed the exploitation of the surface diffusivity to increase protein uptake, transcending the customary perception that it limits protein uptake.

Results and Discussion

Surface Diffusivity of a Protein Depends Inversely on Its Binding Strength. Although qualitative confirmation of the importance of surface diffusion in protein chromatography is provided by confocal microscopy observations, quantitative estimates of D_s are usually obtained by fitting column data to mechanistic models. Models that account only for pore diffusion provide acceptable uptake predictions for small proteins such as lysozyme (32) and cytochrome *c* (*SI Appendix*, Fig. S2) but not for mAbs (ref. 33 and *SI Appendix*, Fig. S2). Incorporation of surface diffusion leads to a more accurate prediction of protein uptake (*SI Appendix*, Fig. S2), including of mAbs, and allows D_s to be estimated. Fitted surface diffusivities for an mAb on Fractogel SO_3^- at various pH values are plotted in Fig. 1*A* and show a systematic increase with increasing IS, consistent with prior reports (8, 25, 34). The same data plotted against the adsorption equilibrium constant, K_{eq}, estimated from the same model fits (Fig. 1*C*), collapse onto a single curve, indicating that D_s is primarily a function of protein binding affinity. Similar results are obtained for Fractogel variants with different ligand densities (Fig. 1 *B* and *D*), although the effect of ligand density is smaller than that of pH. The correlation of D_s with K_{eq} is also consistent across resins with differing architectures, specifically ones lacking the polymer functionalization of Fractogel (*SI Appendix*, Fig. S3).

The dependence of the surface diffusivity on parameters such as IS, pH, and resin ligand density is therefore predominantly through their effect on K_{eq}. That the tendency for a protein to diffuse on the adsorbent surface is a function of how strongly it is bound to the surface has been surmised and modeled (9) previously, but the direct relationship of D_s to K_{eq} that emerges from our data provides quantitative confirmation. Operationally, the results in Fig. 1 *A* and *B* show that D_s can be modulated by changing the IS or by using a resin with a different ligand density. The very low values of D_s below 50–70 mM IS reflect the strong adsorption in the absence of significant screening of Coulombic attraction. This effect has been modeled on IEX resins (9, 34) and observed across enzyme-immobilized substrates (8).

In IEX operation, the lower D_s at a lower IS results in slower uptake into particles in the column, as a result of which more protein leaves the column prior to saturation of the resin beads (35, 36); this is seen in the shallowness of the protein uptake curves presented in Fig. 1*E*. To avoid unnecessary product loss in preparative operations, the protein feed is usually stopped before this breakthrough occurs and the amount of protein bound at this point is termed the dynamic binding capacity (DBC). The steeper the breakthrough is, the smaller the difference between the equilibrium and DBCs. However, the benefit of the sharper breakthrough that results from higher D_s at higher IS is significantly offset by the associated lower equilibrium capacity, shown in the table next to Fig. 1*E*.

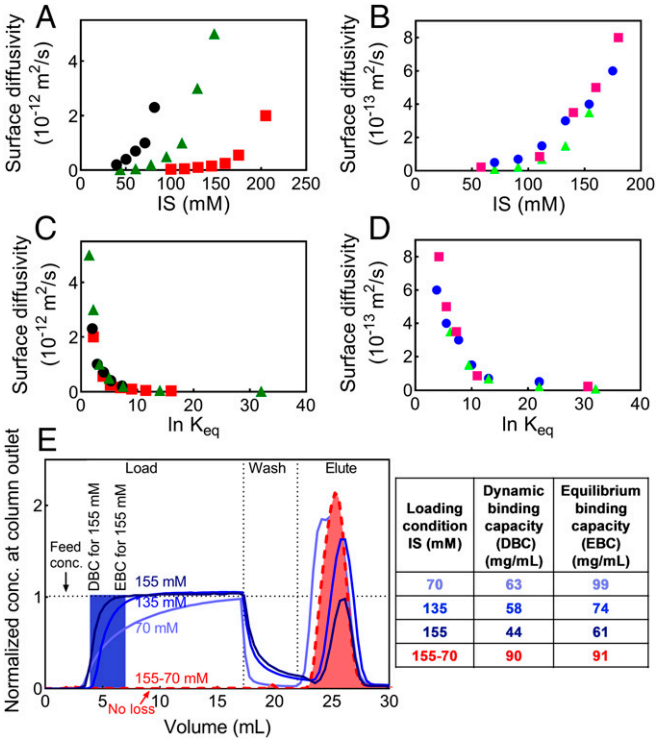

Loading condition IS (mM)	Dynamic binding capacity (DBC) (mg/mL)	Equilibrium binding capacity (EBC) (mg/mL)
70	63	99
135	58	74
155	44	61
155-70	90	91

Fig. 1. MAb surface diffusivities estimated by fitting column breakthrough curves at various pH values (*A* and *C*) and resin ligand densities (*B* and *D*), plotted against buffer IS and the estimated protein binding equilibrium constant. (*E*) MAb breakthrough and elution curves at 70-, 135-, and 155 mM IS as well as for a 155–70-mM gradient, all at pH 5. The binding capacities for the samples in *E* are shown in the table. Symbols: (*A* and *C*) standard resin: black circles, pH 6.0; green triangles, pH 5.5; red squares, pH 5.0. (*B* and *D*) pH 5.5: blue circles, low; magenta squares, standard; green triangles, high ligand-density resin.

Loading by a Decreasing Salt and Protein Gradient Promotes Faster and More Homogeneous mAb Uptake. In order to leverage the relation between D_s and K_{eq}, the binding strength during sample loading was modulated by changing the buffer IS to obtain faster protein surface diffusion initially, but with the final IS low enough so as not to compromise the DBC. Specifically, the IS and the protein concentration in the feed were decreased linearly during sample loading onto the column, with model simulations used to optimize the protein and salt concentration ranges. Using the optimal IS range of 155–70 mM, the experimental protein concentration exiting the column is shown for the mAb at pH 5.0 in Fig. 1*E* in red, while the simulated amounts bound to the column are shown vs. column position and time in Fig. 2 *A* and *B* for isocratic (constant IS) and gradient loading, respectively. The gradient method significantly delayed protein breakthrough (Fig. 1*E*) and resulted in a 43% higher DBC than at 70 mM IS, as evident from the larger area under the blue surface at a given time in Fig. 2*B* than in Fig. 2*A*. Overall, faster and more sustained protein uptake (Fig. 2*B*) is achieved compared to that using isocratic loading (Fig. 2*A*) at a lower IS (35, 37, 38). This is consistent with a higher D_s value during the early stages of protein loading as a result of the higher IS.

Characterization of the gradient-loaded resin by confocal microscopy and SANS provides microscopic and nanoscopic information on the intraparticle protein distribution that confirms the role of surface diffusion. Confocal micrographs of resin beads

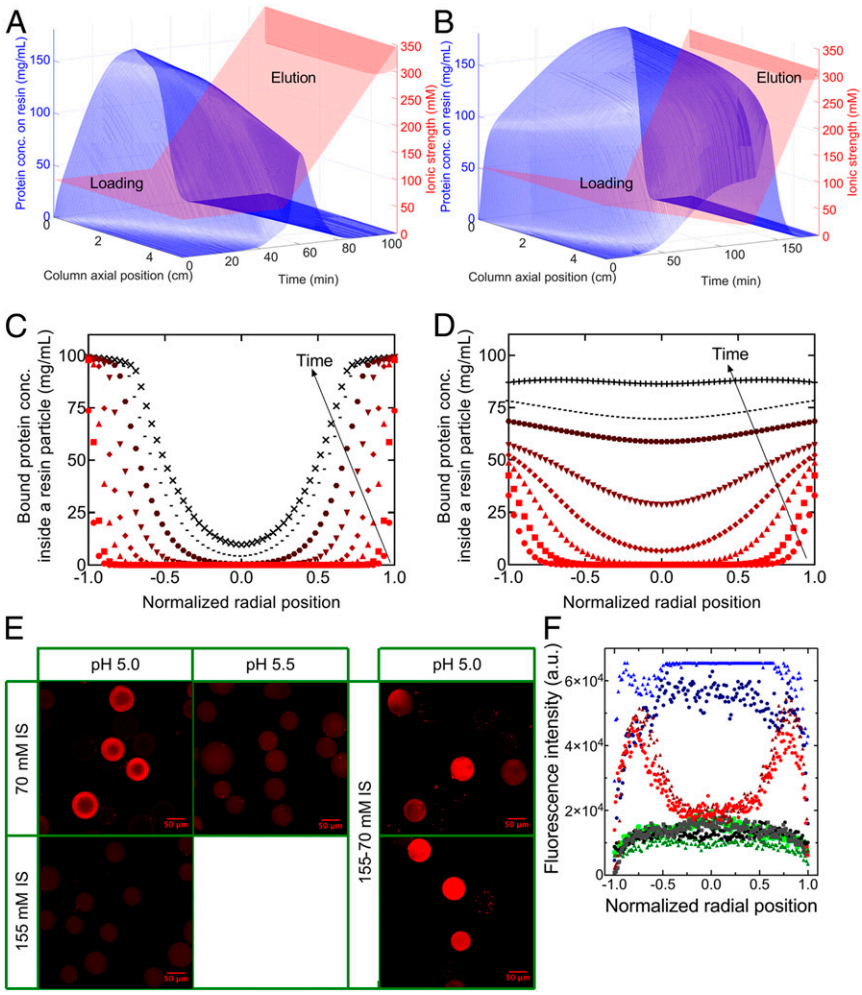

Fig. 2. Simulated column-bound protein concentrations during sample loading at pH 5 with a buffer IS of 70 mM (*A*) or a 155–70-mM gradient (*B*), and subsequent elution, all as functions of time and column axial position. The corresponding simulated bound protein concentrations within individual resin beads at the column entrance are shown in *C* and *D*. Time points in *C* correspond to 0.7 (red circles), 1.5 (red squares), 3.7 (red triangles), 7.3 (red diamonds), 14.6 (maroon triangles), 25.6 (maroon circles), 36.6 (black dashes), and 44.1 min (black crosses), respectively, and in *D* to 0.7 (red circles), 1.5 (red squares), 3.7 (red triangles), 7.3 (red diamonds), 14.6 (maroon triangles), 36.6 (maroon circles), 58.6 (black dashes), and 146.5 min (black crosses), respectively. Resin particles were removed from the column and visualized (*E*) after loading of fluorescently labeled protein in an equivalent manner to the simulation. In both simulations and experiments, the mAb was loaded onto the Fractogel SO_3^- (M) column until the DBC was reached. The fluorescence intensity profiles for two particles from each image in *E* are plotted as a function of normalized radial position in *F*. Symbols in *F*: red circles and maroon triangles, 70 mM, pH 5.0; green triangles and chartreuse squares, 155 mM, pH 5.0; black circles and gray squares, 70 mM, pH 5.6; navy blue circles and royal blue triangles, 155–70 mM, pH 5.0.

imaged after loading of fluorescently labeled mAb to the DBC under different conditions are shown in Fig. 2*E*. Isocratic loading at low IS (70 mM, pH 5.0) gives rise to a core–shell protein distribution, with very little protein near the center of the particle (18–20). In contrast, loading at high IS (155 mM, pH 5.0) leads to a more uniform protein distribution, but at the cost of a lower total capacity. A similar contrast is seen upon a pH increase from 5.0 to 5.5 at 70 mM IS (Fig. 2*E*) because this decreases the mAb's net charge and hence weakens its affinity to the resin, thereby increasing its D_s (Fig. 1*A*). Unlike for isocratic loading, gradient-loaded resin beads show the highest amount of bound protein with a quite uniform protein distribution (Fig. 2*E*). The radial intensity profiles after protein loading shown in Fig. 2*F* are in very good agreement with the corresponding simulated radial protein distributions shown in Fig. 2 *C* and *D*, specifically the higher protein concentration or intensity at the shell of the particle when the protein is loaded isocratically at 70 mM IS, with the core remaining undersaturated.

The impact of surface diffusion on the protein distribution was further probed on the nanoscale—structural features 1–100s of nanometers—using SANS. Details of the acquisition, interpretation, and modeling of scattering spectra are included in *SI Appendix*. Briefly, the resin structure was studied with and without adsorbed protein using the coherent scattering contribution arising from the contrast between the D_2O-buffer-filled pores and the hydrogen-containing protein and resin. The scattering spectra of resin beads with and without protein are shown in Fig. 3 *A* and *B* before and after subtraction of incoherent background scattering and scaling, respectively. The large incoherent scattering cross-section of the hydrogen atom dominates the incoherent scattering manifested in the baselines of the spectra. This correlates to the protein content (Fig. 3 *A*, *Inset*) in equivalently D_2O-exchanged samples in which the protein is the variable source of hydrogen.

SANS measurements on the neat resin (*SI Appendix*, Fig. S5*A*) showed no detectable changes in resin structure as a function of IS in the range of the chromatographic salt gradient over the length-scale range 13–1,500 Å. This is consistent with the small (5%) increase in Fractogel porosity (39) and virtually overlapping small-angle X-ray scattering spectra (40) reported for

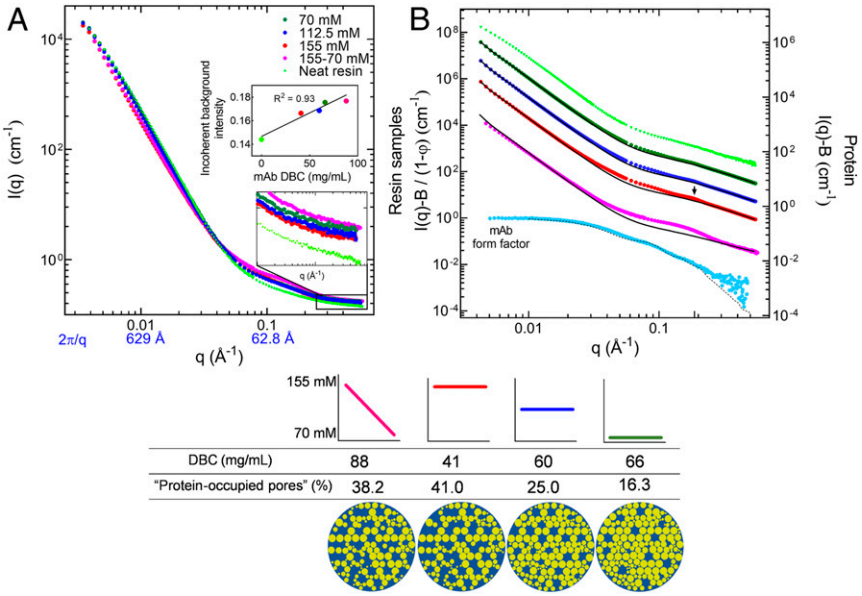

Fig. 3. SANS spectra for the mAb-loaded Fractogel SO^-_3 (M) resins. The mAb was loaded onto the resin isocratically at 70-, 112.5-, and 155-mM IS, as well as using an IS gradient of 155–70 mM, until the DBC was reached. The spectra are shown in *A* with the lower and upper insets showing the background incoherent scattering and its correlation to the DBC, respectively. The length scales corresponding to the *q* space are provided in blue below the abscissa. The same spectra after background reduction and scaling are shown in *B* along with the volume-fraction-adjusted sum model (black line) for each curve. The background-reduced spectrum (dotted blue curve) of 7.4 mg/mL pure mAb in 100-mM sodium acetate buffer in D_2O (right ordinate) is included to capture the mAb form factor. The dashed line is the scattering spectrum of an IgG1 molecule predicted by CRYSON using the Protein Data Bank ID code 1IGY (62). Apart from the mAb solution, successive curves are shifted by a factor of 6 for clarity. The arrows at 0.187 $Å^{-1}$ point to a peak of which the position is interpreted to indicate the nearest-neighbor distance. The lower part of the figure shows the DBC and the percentage of "protein-occupied pores," along with its pictorial depiction, for each loading condition.

buffer IS increases of 500 and 80 mM, respectively. Therefore, changes in the SANS spectra in the protein-loaded samples can be attributed to protein effects, not to the neat resin. A simple yet quantitative interpretation of both the neat resin and protein-loaded samples was obtained by fitting the respective spectra to a physical model based on the sum of polydisperse hard spheres (41) and the Lorentz model (42, 43), representing the buffer-filled intraparticle pores and the hydrated polymer network, respectively (*SI Appendix*, Fig. S4). For the neat resin (*SI Appendix*, Fig. S5*B*), this model, termed the "sum model," fits the spectra with physically meaningful parameter values (*SI Appendix*, Table S4).

The model also fits the spectra for the protein-adsorbed samples in the low-*q* region (<0.03 $Å^{-1}$; length scales >200 Å and therefore comparable to pore sizes) (Fig. 3*B*); the key fitting parameter represents the fraction of the "hard-sphere" (pore) volume that is now occupied primarily by protein rather than D_2O. Protein-filled pores attain a similar scattering length density (SLD) to that of the polymer network, hence neutrons detect an effective reduction in the pore volume fraction upon protein adsorption, as illustrated schematically at the bottom of Fig. 3*B*. This is reasonable as an SLD within 15% of the fitted value for the resin matrix was reported for a D_2O-exchanged mAb (44). The sum model takes a binary view of a pore as either "empty" or "filled" for ease of analysis. Although realistically there is a gradient between empty and filled states, this approach allows the sum model to enable quantitative analysis of SANS data to obtain insights into the protein distribution on the pore scale.

Comparing the fitted fraction of protein-filled pores for the isocratic loading experiments at three different IS values shows that the fraction varies inversely with DBC. Therefore, pore occupancy reflects not the total protein loading but rather the distribution of protein within the beads, which is less uniform at lower IS values, i.e., when surface diffusion is slower. This distribution on the pore level is consistent with the inference from the confocal microscopy data, e.g., the core–shell adsorption pattern seen at 70 mM (Fig. 2*E*) is manifested as low pore occupancy in the SANS data. Therefore, the confocal micrographs, SANS spectra, and column simulations all demonstrate that the higher the surface diffusivity during loading, the more uniform the protein distribution that is seen at the column (centimeters), bead (tens of micrometers), and pore (tens of nanometers) length scales. The gradient loading combines this surface diffusion effect with the increased equilibrium capacity at lower IS, resulting in 2.3× higher pore occupancy than for the 70-mM sample, with a 43% higher DBC.

The higher-*q* regions of the SANS spectra indicate additional features of the protein distribution. The discrepancies in the fits in Fig. 3*B* between 0.03 and 0.3 $Å^{-1}$ (209–20.9 Å) reflect the scattering from the individual protein molecules and their arrangement with respect to one another, which is not accounted for in the sum model. The sum model accounts for the presence of protein only via the contribution of the protein-filled pores. The individual molecules [~137 × 83 Å (45)] collectively contribute to the scattering intensity through their shape via the form factor, shown in light blue in Fig. 3*B*. These contributions may be modulated by interprotein correlations, termed the structure factor, which may be significant given the mAb loadings of 44–90 mg/mL, with actual local concentrations effectively much higher. Indeed, the scattering spectrum of the sample with the highest local protein density and potentially largest interprotein correlations, from loading at 70 mM IS, seemingly deviates the least from the model fit between 0.03 and 0.2 $Å^{-1}$ (Fig. 3*B*), probably due to the masked form factor. A subtle peak at 0.186 $Å^{-1}$ on the 155-mM sample (arrow in Fig. 3*B*) suggests a prominent nearest-neighbor distance of 34 Å between the mAb molecules, similar to the 37 Å reported for mAb-sorbed chromatographic resins (46) and the 31 Å reported for a frozen

171 mg/mL mAb solution (47). Given that the radius of gyration of a typical mAb is 48 Å (48, 49), an interprotein distance of 34 Å suggests interdigitation of subunits (49). The equivalent peak for the gradient loading sample is broader, which may suggest a broader distribution of nearest-neighbor distances, per our hypothesis that the gradient method promotes mAb surface diffusion in the resin bead. A broad distribution of protein spacing in a chromatographic resin with a large surface area may mitigate surface-mediated (50, 51) and self-associated (52–56) protein conformational changes.

The Leverage Provided by Manipulating Surface Diffusion Increases with Increasing Protein Size and Affinity. The utility of the gradient-loading method was evaluated for two different proteins and for a set of resins differing in ligand density (*SI Appendix*, Table S2), which has been shown to affect the adsorption affinity (40). Our hypothesis was that situations in which baseline transport rates were lower—larger proteins with lower free-solution diffusivities and systems with higher adsorption affinity—would benefit more from the gradient-loading method.

The behavior of the mAb studied above was investigated on ligand-density variants of the same Fractogel resin used previously (40, 57). Fig. 4 *A* and *B* show SANS spectra for the neat and mAb-laden low- and high-density variants, with the mAb-laden samples prepared using both isocratic and gradient loading, albeit over different IS ranges; the optimal IS range is narrower for the low-density resin because less screening is needed to modulate the weaker adsorption. For the high-density resin (Fig. 4*B*) at 35 mM IS, the neat and mAb-laden spectra nearly overlap. The lower surface diffusivity in the high-density case produces a core–shell adsorption structure with adsorption mainly around the bead periphery, so the central core of the bead retains the character of the neat resin. This rationale is consistent with the lower surface diffusivity reported for strongly adsorbed amyloid β-peptide on highly hydrophilic surfaces (3). In contrast, with gradient loading, the spectrum of the mAb-laden sample deviates significantly from that of the neat resin and 3.5× more mAb is taken up than at 35-mM IS, showing the appreciable benefit due to the enhanced surface diffusion.

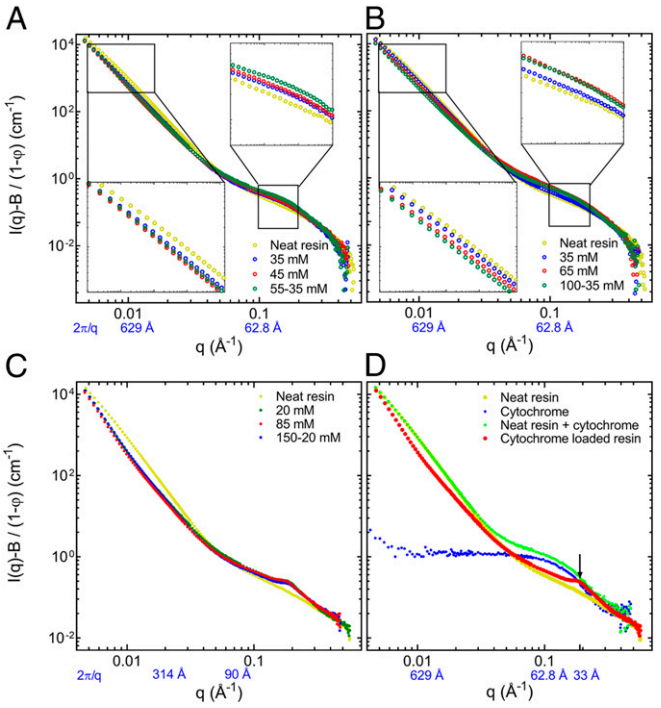

Fig. 4. SANS spectra after background subtraction and scaling are shown for the mAb-loaded resins of low (*A*) and high (*B*) ligand densities, and cytochrome *c*-loaded resins (*C* and *D*) of high ligand density. The length scales corresponding to the *q* values are provided in blue below the abscissa. (*A*) MAb masses of 22.4, 29.4, and 45.4 mg were loaded per milliliter of low ligand-density resin using buffer IS of 35 mM, 45 mM, and a gradient of 55–35 mM at pH 5.5, respectively, until the DBC was reached. Similar data at pH 5.5 are shown in *B* for the high ligand-density resin with mAb loaded at 35 mM (13.6 mg/mL), 65 mM (31.4 mg/mL), and 100–35 mM (46.8 mg/mL) IS, and in *C* with cytochrome *c* loaded at 20 mM (65.4 mg/mL), 85 mM (75.6 mg/mL) and 150–20 mM (73.5 mg/mL) IS. (*D*) The scattering spectrum for cytochrome *c*-loaded resin at 20 mM IS (65.4 mg/mL of resin) is shown in red, while the separate spectra for the neat resin and the cytochrome *c* solution (65.4 mg/mL) are shown in yellow and blue, respectively. The mathematical sum of the spectra for the neat resin and the cytochrome *c* solution is shown in green. The arrow points to a pronounced peak, the position of which is interpreted to indicate the nearest-neighbor distance.

For the low ligand-density resin, in contrast, all modes of protein loading (Fig. 4*A*) result in overlapping spectra in the low-*q* region, indicating less promotion of protein surface diffusion during gradient loading in this situation of lower binding affinity. In the high-*q* regions (<200 Å), where the presence of protein molecules and interactions among them contribute to the scattered intensity (46, 47, 58), the nearest-neighbor peak between 126 and 29 Å grows with increasing protein content in the different samples, suggesting similar protein spatial distributions. However, the corresponding peak ordering does not depend on protein content for the high-density case as protein distributions differ among samples due to differences in surface diffusion during sample loading.

The benefit gained by manipulating protein surface diffusion depends on its contribution to mass transport relative to that of protein diffusion in the fluid-filled pore space. While the surface diffusivity depends on the binding affinity, the pore diffusivity follows the free-solution diffusivity in varying inversely with the protein hydrodynamic radius, except if pore constriction is severe. SANS spectra of cytochrome *c*-laden samples on the high ligand-density resin acquired after loading to the DBC using the isocratic and gradient methods (Fig. 4*C*) are all similar, in contrast to the mAb-laden samples (Fig. 4*B*). Cytochrome *c* is smaller than a mAb by about a factor of 10 in molecular mass and about a factor of 3 in hydrodynamic radius, giving it much higher free-solution and pore diffusivities. As a result, pore diffusion appears adequate to lead to a fairly uniform intraparticle distribution even in the absence of enhanced surface diffusion. The effect of protein size on intraparticle distribution was also seen for thyroglobulin (660 kDa), which adsorbed predominantly at the particle surface (59) due to limited mobility at a low IS but adsorbed more homogeneously at a higher IS.

The deviations in Fig. 4*C* between the spectra for the protein-laden and neat samples are evaluated systematically in Fig. 4*D*, for the sample loaded at 20 mM IS. The protein form factor corresponding to the amount of bound cytochrome *c* (blue) is added to the spectrum for the neat resin (yellow) and plotted along with the experimental spectrum (red). The experimental spectrum is lower in the low-*q* region because the adsorbed cytochrome *c* augments the resin's fractal features in the 200–1,500-Å length-scale range; this effect is opposite to that reported for lysozyme adsorbed in S HyperCel (46, 58), a resin with a significantly different architecture. In the high-*q* region, a clear peak at a nearest-neighbor spacing of ~33 Å is present for all three protein-laden samples in Fig. 4*C*. The similar intermolecular spacing at different sample loading conditions supports our rationale that the higher pore diffusivity of cytochrome *c* reduces the dependence of transport properties on the binding affinity because of the reduced importance of surface diffusion.

Conclusions

The absence of a consensus regarding the role of surface diffusion in IEX of proteins is likely due in part to the variability of the surface diffusivity with solution conditions. We have shown that the surface diffusivity is a function of the adsorption equilibrium constant K_{eq}, independent of the buffer IS and pH and the resin ligand density. We have furthermore exploited this finding by introducing a method of column loading in which transient manipulation of the buffer IS can allow an appreciable increase in the protein surface diffusivity and hence in the protein saturation efficiency and resin utilization. The resulting increase in DBC of as much as >40% allows loading up to near the equilibrium binding capacity. Confocal microscopy and SANS measurements provide complementary evidence that the DBC increase is accompanied by improved and more homogeneous adsorbent utilization. A more widespread spatial distribution of adsorbed mAb, particularly in a resin such as Fractogel in which additional adsorption capacity has been introduced by polymer functionalization, may result in a reduction in surface-mediated (50, 51) and self-associated (52–56) conformational changes. The results presented here provide an indication of where the approach can have the most impact, namely for larger proteins under high-affinity binding conditions that are amenable to attenuation by manipulation of the solution conditions. Our observations and broadly applicable approaches can help evaluate systems where protein-adsorbent interaction is mass-transfer limited, such as other adsorptive systems, biointerfaces, and biosensors. Beyond capturing the structural features at the end of uptake as has been done here, of particular value would be distinguishing pore and surface diffusion mechanisms in situ in the pore space in real time.

Materials and Methods

Chromatography Experiments. Protein (3–6 mg/mL) was loaded onto a 0.35 mL (0.3-cm inner diameter) column packed with Fractogel SO_3^- M-type resin (*SI Appendix*, Table S1) across a gradient of 100% buffer A (155- or 100-mM sodium acetate, pH 5–5.5) to 100% buffer B (0 mg/mL of protein in 70 or 35-mM sodium acetate, pH 5–5.5) at a flow rate of 0.17 mL/min; the two gradients used were 155–70-mM sodium acetate and 100–35-mM sodium acetate. The column effluent was monitored by UV absorbance at 280 nm.

Mechanistic Modeling. The general rate model was coupled with a colloidal isotherm model to describe the partitioning of solute between the liquid and solid phases. This model accounts for convection, axial dispersion, external mass transfer to the particle and pore and surface diffusion inside the particle. All simulations were performed using the Chromatography Analysis and Design Toolkit (CADET) (60).

Confocal Microscopy. A solution of Cy3.5-labeled mAb (3–6 mg/mL) with a 3% molar labeling ratio was loaded onto the chromatography column. The resin slurry was removed and stored at 4 °C for 12–24 h before visualization on an inverted Zeiss 710 confocal microscope using a 20× Plan-Apochromat (0.8 numerical aperture) M27 objective.

SANS. Protein was loaded onto a packed column as described above, but in a buffer prepared from 99% D_2O. The resin slurry was stored for 24–48 h at 4 °C before spectral acquisition which was performed in quartz window cells with a path length of 1 mm using the 30-m NG7 SANS instrument at the National Center for Neutron Research. Raw data were reduced using IGOR Pro following the standard procedure (61).

Further details of materials, equipment, and methods used are provided in *SI Appendix*.

Data Availability. *SI Appendix* includes files and tables providing experimental data and parameter estimates.

ACKNOWLEDGMENTS. We thank Stijn H. S. Koshari for valuable discussions, and Amgen and EMD Millipore for providing the mAb and the ligand-density variant resins, respectively. We also thank Prof. Eric von Lieres of Forschungszentrum Jülich for making CADET available for the simulations. This work utilized the neutron research facility at the National Center for Neutron Research at the National Institute of Standards and Technology of the US Department of Commerce, and the BioImaging Facility at the Delaware Biotechnology Institute, supported in part by the National Institutes of Health Grant P20 GM103446.

1. I. Brouwer *et al.*, Sliding sleeves of XRCC4-XLF bridge DNA and connect fragments of broken DNA. *Nature* **535**, 566–569 (2016).
2. Y. C. Lin, C. Li, Z. Fakhraai, Kinetics of surface-mediated fibrillization of amyloid-β (12–28) peptides. *Langmuir* **34**, 4665–4672 (2018).
3. L. Shen, T. Adachi, D. Vanden Bout, X. Y. Zhu, A mobile precursor determines amyloid-β peptide fibril formation at interfaces. *J. Am. Chem. Soc.* **134**, 14172–14178 (2012).
4. H. Wang *et al.*, Microfluidic immunosensor based on stable antibody-patterned surface in PMMA microchip. *Electrochem. Commun.* **10**, 447–450 (2008).
5. N. Kaneki *et al.*, Electrochemical enzyme immunoassay using sequential saturation technique in a 20-μl capillary: Digoxin as a model analyte. *Anal. Chim. Acta* **287**, 253–258 (1994).
6. B. Johnsson, S. Löfås, G. Lindquist, Immobilization of proteins to a carboxymethyldextran-modified gold surface for biospecific interaction analysis in surface plasmon resonance sensors. *Anal. Biochem.* **198**, 268–277 (1991).
7. H. Schmidt-Traub, *Preparative Chromatography: of Fine Chemicals and Pharmaceutical Agents* (John Wiley & Sons, 2005).
8. B. E. Feller, J. T. Kellis, Jr, L. G. Cascão-Pereira, C. R. Robertson, C. W. Frank, The role of electrostatic interactions in protease surface diffusion and the consequence for interfacial biocatalysis. *Langmuir* **26**, 18916–18925 (2010).
9. J. A. Wesselingh, J. C. Bosma, Protein ion-exchange adsorption kinetics. *AIChE J.* **47**, 1571–1580 (2001).
10. I. Medved', R. Černý, Surface diffusion in porous media: A critical review. *Microporous Mesoporous Mater.* **142**, 405–422 (2011).
11. J. G. Choi, D. D. Do, H. D. Do, Surface diffusion of adsorbed molecules in porous media: Monolayer, multilayer, and capillary condensation regimes. *Ind. Eng. Chem. Res.* **40**, 4005–4031 (2001).
12. H. Yoshida, M. Yoshikawa, T. Kataoka, Parallel transport of BSA by surface and pore diffusion in strongly basic chitosan. *AIChE J.* **40**, 2034–2044 (1994).
13. D. Wang, H. Y. Chin, C. He, M. P. Stoykovich, D. K. Schwartz, Polymer surface transport is a combination of in-plane diffusion and desorption-mediated flights. *ACS Macro Lett.* **5**, 509–514 (2016).
14. D. Wang, C. He, M. P. Stoykovich, D. K. Schwartz, Nanoscale topography influences polymer surface diffusion. *ACS Nano* **9**, 1656–1664 (2015).
15. J. Zhao, S. Granick, Polymer lateral diffusion at the solid-liquid interface. *J. Am. Chem. Soc.* **126**, 6242–6243 (2004).
16. J. Zhao, S. Granick, How polymer surface diffusion depends on surface coverage. *Macromolecules* **40**, 1243–1247 (2007).
17. J. Rybka, A. Höltzel, U. Tallarek, Surface diffusion of aromatic hydrocarbon analytes in reversed-phase liquid chromatography. *J. Phys. Chem. C* **121**, 17907–17920 (2017).
18. K. Miyabe, G. Guiochon, Surface diffusion in reversed-phase liquid chromatography. *J. Chromatogr. A* **1217**, 1713–1734 (2010).
19. J. Rybka, A. Höltzel, S. M. Melnikov, A. Seidel-Morgenstern, U. Tallarek, A new view on surface diffusion from molecular dynamics simulations of solute mobility at chromatographic interfaces. *Fluid Phase Equilib.* **407**, 177–187 (2016).
20. F. Gritti, G. Guiochon, Mass transfer mechanism in chiral reversed phase liquid chromatography. *J. Chromatogr. A* **1332**, 35–45 (2014).
21. F. Gritti, G. Guiochon, Importance of sample intraparticle diffusivity in investigations of the mass transfer mechanism in liquid chromatography. *AIChE J.* **57**, 346–358 (2011).
22. R. D. Tilton, C. R. Robertson, A. P. Gast, Lateral diffusion of bovine serum albumin adsorbed at the solid-liquid interface. *J. Colloid Interface Sci.* **137**, 192–203 (1990).
23. I. Michaeli, D. R. Absolom, C. J. Van Oss, Diffusion of adsorbed protein within the plane of adsorption. *J. Colloid Interface Sci.* **77**, 586–587 (1980).
24. H. Nygren, S. Alaeddin, I. Lundström, K. E. Magnusson, Effect of surface wettability on protein adsorption and lateral diffusion. Analysis of data and a statistical model. *Biophys. Chem.* **49**, 263–272 (1994).
25. J. E. Basconi, G. Carta, M. R. Shirts, Multiscale modeling of protein adsorption and transport in macroporous and polymer-grafted ion exchangers. *AIChE J.* **60**, 3888–3901 (2014).
26. M. C. Stone, Y. Tao, G. Carta, Protein adsorption and transport in agarose and dextran-grafted agarose media for ion exchange chromatography: Effect of ionic strength and protein characteristics. *J. Chromatogr. A* **1216**, 4465–4474 (2009).
27. R. Corbett *et al.*, Structure and protein adsorption mechanisms of clean and fouled tentacle-type anion exchangers used in a monoclonal antibody polishing step. *J. Chromatogr. A* **1278**, 116–125 (2013).
28. K. Miyabe, G. Guiochon, Kinetic study of the mass transfer of bovine serum albumin in anion-exchange chromatography. *J. Chromatogr. A* **866**, 147–171 (2000).
29. L. E. Weaver, G. Carta, Protein adsorption on cation exchangers: Comparison of macroporous and gel-composite media. *Biotechnol. Prog.* **12**, 342–355 (1996).
30. J. Woodcock, R. Woosley, The FDA critical path initiative and its influence on new drug development. *Annu. Rev. Med.* **59**, 1–12 (2008).
31. S. Y. Wu, A. Green, *Projection of Chronic Illness Prevalence and Costs Inflation* (RAND Corp., 2000).

32. S. R. Gallant, S. Vunnum, S. M. Cramer, Optimization of preparative ion-exchange chromatography of proteins: Linear gradient separations. *J. Chromatogr. A* **725**, 295–314 (1996).
33. V. Kumar, S. Leweke, E. von Lieres, A. S. Rathore, Mechanistic modeling of ion-exchange process chromatography of charge variants of monoclonal antibody products. *J. Chromatogr. A* **1426**, 140–153 (2015).
34. A. M. Lenhoff, Multiscale modeling of protein uptake patterns in chromatographic particles. *Langmuir* **24**, 5991–5995 (2008).
35. C. Harinarayan *et al*., An exclusion mechanism in ion exchange chromatography. *Biotechnol. Bioeng.* **95**, 775–787 (2006).
36. S. R. Dziennik, E. B. Belcher, G. A. Barker, A. M. Lenhoff, Effects of ionic strength on lysozyme uptake rates in cation exchangers. I: Uptake in SP Sepharose FF. *Biotechnol. Bioeng.* **91**, 139–153 (2005).
37. B. D. Bowes, A. M. Lenhoff, Protein adsorption and transport in dextran-modified ion-exchange media. III. Effects of resin charge density and dextran content on adsorption and intraparticle uptake. *J. Chromatogr. A* **1218**, 7180–7188 (2011).
38. A. Ljunglöf *et al*., Ion exchange chromatography of antibody fragments. *Biotechnol. Bioeng.* **96**, 515–524 (2007).
39. H. Thomas *et al*., Role of tentacles and protein loading on pore accessibility and mass transfer in cation exchange materials for proteins. *J. Chromatogr. A* **1285**, 48–56 (2013).
40. R. Bhambure *et al*., Ionic strength-dependent changes in tentacular ion exchangers with variable ligand density. II. Functional properties. *J. Chromatogr. A* **1506**, 55–64 (2017).
41. W. L. Griffith, R. Triolo, A. L. Compere, Analytical scattering function of a polydisperse Percus-Yevick fluid with Schulz- (Gamma -) distributed diameters. *Phys. Rev. A Gen. Phys.* **35**, 2200–2206 (1987).
42. P. Debye, H. R. Anderson, H. Brumberger, Scattering by an inhomogeneous solid. II. the correlation function and its application. *J. Appl. Phys.* **28**, 679–683 (1957).
43. P. Debye, A. M. Bueche, Scattering by an inhomogeneous solid. *J. Appl. Phys.* **20**, 518–525 (1949).
44. O. Dunne *et al*., Matchout deuterium labelling of proteins for small-angle neutron scattering studies using prokaryotic and eukaryotic expression systems and high cell-density cultures. *Eur. Biophys. J.* **46**, 425–432 (2017).
45. Y. H. Tan *et al*., A nanoengineering approach for investigation and regulation of protein immobilization. *ACS Nano* **2**, 2374–2384 (2008).
46. S. H. S. Koshari, N. J. Wagner, A. M. Lenhoff, Effects of resin architecture and protein size on nanoscale protein distribution in ion-exchange media. *Langmuir* **34**, 673–684 (2018).
47. J. E. Curtis *et al*., Small-angle neutron scattering study of protein crowding in liquid and solid phases: Lysozyme in aqueous solution, frozen solution, and carbohydrate powders. *J. Phys. Chem. B* **116**, 9653–9667 (2012).
48. E. J. Yearley *et al*., Observation of small cluster formation in concentrated monoclonal antibody solutions and its implications to solution viscosity. *Biophys. J.* **106**, 1763–1770 (2014).
49. M. M. Castellanos *et al*., Role of molecular flexibility and colloidal descriptions of proteins in crowded environments from small-angle scattering. *J. Phys. Chem. B* **120**, 12511–12518 (2016).
50. A. Voitl, A. Butté, M. Morbidelli, Behavior of human serum albumin on strong cation exchange resins: I. Experimental analysis. *J. Chromatogr. A* **1217**, 5484–5491 (2010).
51. J. Guo, G. Carta, Unfolding and aggregation of monoclonal antibodies on cation exchange columns: Effects of resin type, load buffer, and protein stability. *J. Chromatogr. A* **1388**, 184–194 (2015).
52. J. Liu, M. D. H. Nguyen, J. D. Andya, S. J. Shire, Reversible self-association increases the viscosity of a concentrated monoclonal antibody in aqueous solution. *J. Pharm. Sci.* **94**, 1928–1940 (2005).
53. H. Nishi *et al*., Phase separation of an IgG1 antibody solution under a low ionic strength condition. *Pharm. Res.* **27**, 1348–1360 (2010).
54. D. Bethea *et al*., Mechanisms of self-association of a human monoclonal antibody CNTO607. *Protein Eng. Des. Sel.* **25**, 531–537 (2012).
55. R. Esfandiary *et al*., A systematic multitechnique approach for detection and characterization of reversible self-association during formulation development of therapeutic antibodies. *J. Pharm. Sci.* **102**, 62–72 (2013).
56. H. Luo *et al*., Effects of salt-induced reversible self-association on the elution behavior of a monoclonal antibody in cation exchange chromatography. *J. Chromatogr. A* **1362**, 186–193 (2014).
57. R. Bhambure, C. M. Gillespie, M. Phillips, H. Graalfs, A. M. Lenhoff, Ionic strength-dependent changes in tentacular ion exchangers with variable ligand density. I. Structural properties. *J. Chromatogr. A* **1463**, 90–101 (2016).
58. S. H. S. Koshari, N. J. Wagner, A. M. Lenhoff, Characterization of lysozyme adsorption in cellulosic chromatographic materials using small-angle neutron scattering. *J. Chromatogr. A* **1399**, 45–52 (2015).
59. M. Zhu, P. Fuks, G. Carta, Protein adsorption in anion exchange resins–Effects of polymer grafting, support structure porosity, and protein size. *J. Chem. Technol. Biotechnol.* **93**, 1948–1958 (2018).
60. E. von Lieres, J. Andersson, A fast and accurate solver for the general rate model of column liquid chromatography. *Comput. Chem. Eng.* **34**, 1180–1191 (2010).
61. S. R. Kline, Reduction and analysis of SANS and USANS data using IGOR Pro. *J. Appl. Cryst.* **39**, 895–900 (2006).
62. L. J. Harris, E. Skaletsky, A. McPherson, Crystallographic structure of an intact IgG1 monoclonal antibody. *J. Mol. Biol.* **275**, 861–872 (1998).